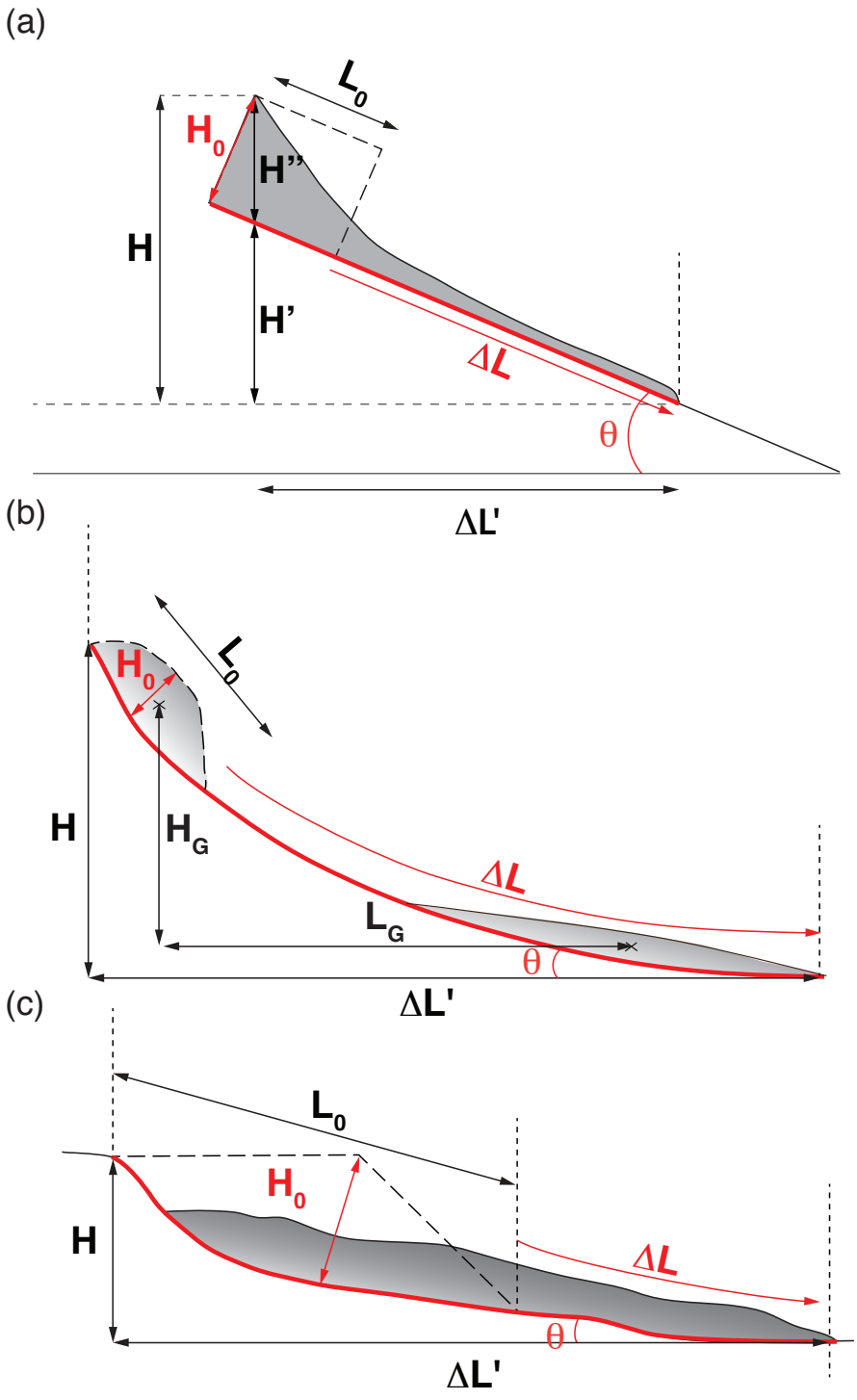

Supplementary Figure 1 **| Landslides metrics in different scenarios.** (a) The dam break scenario, (b) a geometry used in numerical simulations and (c) the most frequent geometry for natural landslides[1]. Here θ is the mean slope angle averaged along the path of the avalanche front from destabilization to the final deposit, H the maximum elevation difference between the deposit front and the maximum elevation of the initial mass, H_0 the maximum initial thickness, L_0 the initial length and ΔL the total length travelled by the front of the landslide. H_G and L_G are the difference in elevation and horizontal distance between the position of the centre of mass of the initial released mass and that of the final deposit, respectively. The dash-lines show the shape of the initial released mass.

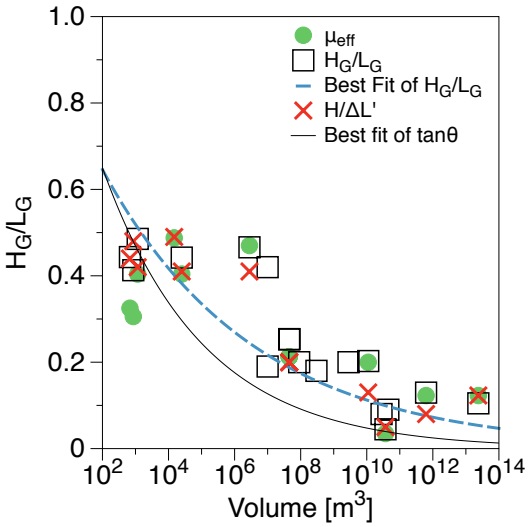

Supplementary Figure 2 **| Centre of mass travel ratio.** Ratio between the difference in elevation and the difference in horizontal distance of the centre of mass from the initial state to the final deposit H_G/L_G as a function of the volume V. H_G/L_G is close to $H/\Delta L'$ (and to μ_{eff}) and decreases with the volume, following a similar trend ($H_G/L_G = V^{-0.0949}$). For the sake of clarity, error bars are not shown but are approximately the size of each symbol on the horizontal axis and twice the size of each symbol on the vertical axis.

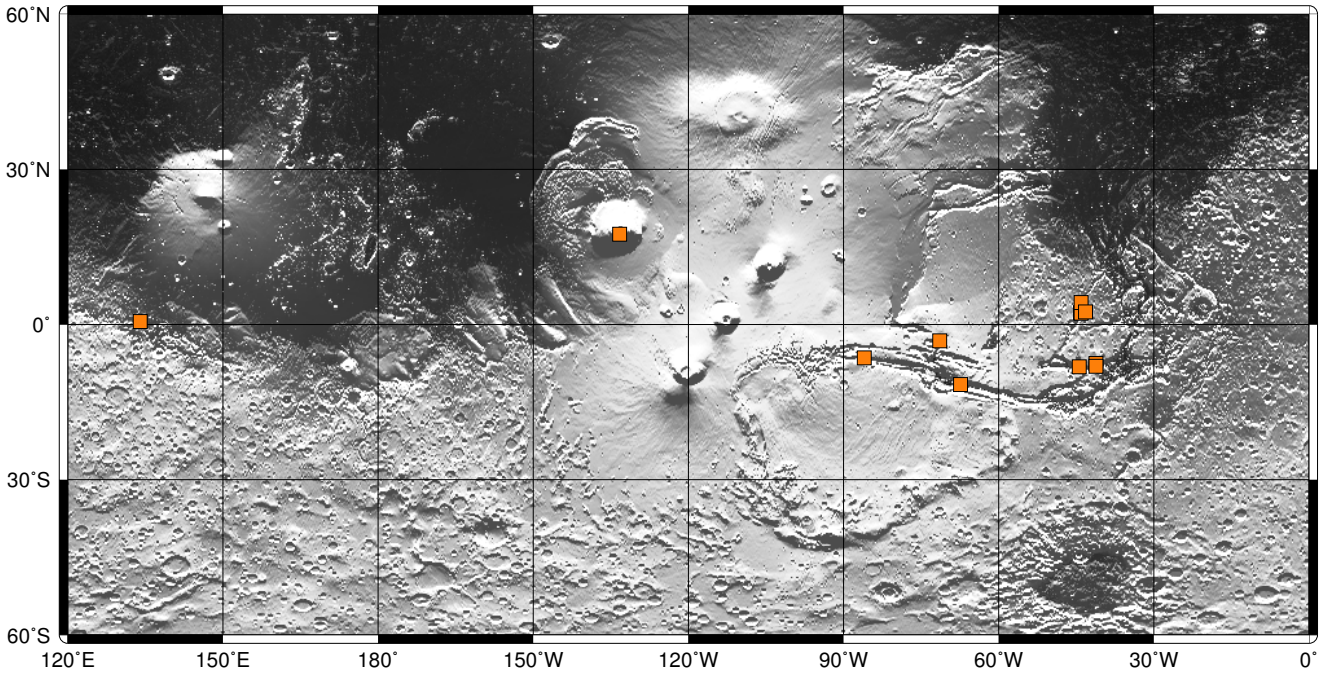

Supplementary Figure 3 **| Location map of Martian landslides studied.** Shaded relief if obtained from MEGDR MOLA.

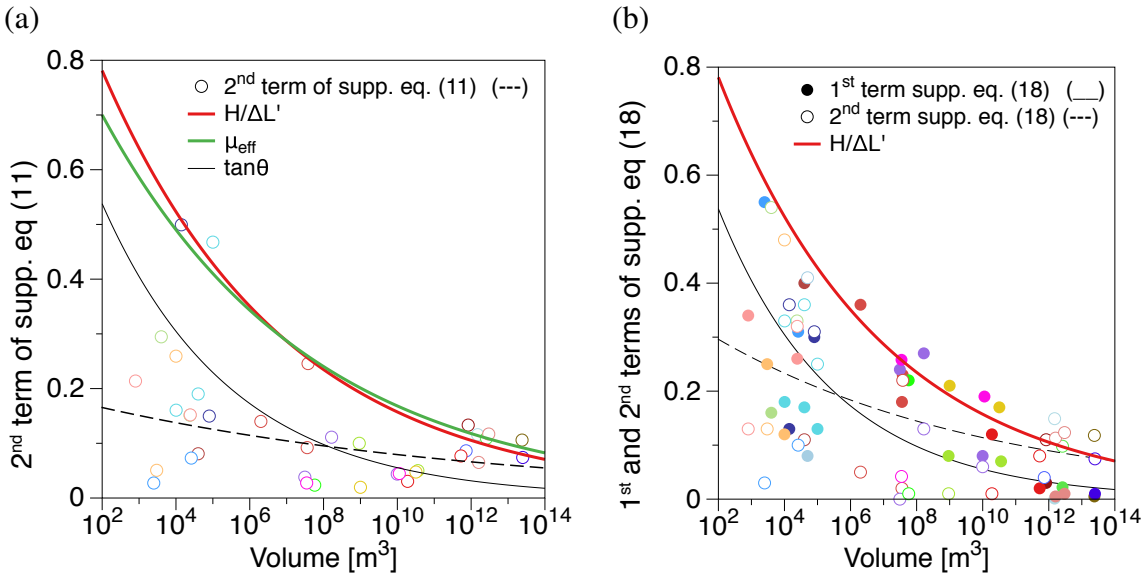

Supplementary Figure 4 **| First and second terms of the Heim's ratio and of the effective friction coefficient equations.** (a) Investigation of the first (only represented by its fit of $\tan\theta$) and second terms (empty circles) of μ_{eff} (supplementary equation (11)) and of their dependence in volume. (b) Investigation of the first term (plain circles) and second term (empty circles) of $H/\Delta L'$ (supplementary equation (18)) and of their dependence on volume. Each landslide is represented by a given colour chosen arbitrarily (but the same on both panels). For (a) and (b), plain and dashed curves are the best fit for the first and second terms, respectively. For the sake of clarity, error bars are not shown but are approximately the size of each symbol on the horizontal axis and twice this size on the vertical axis.

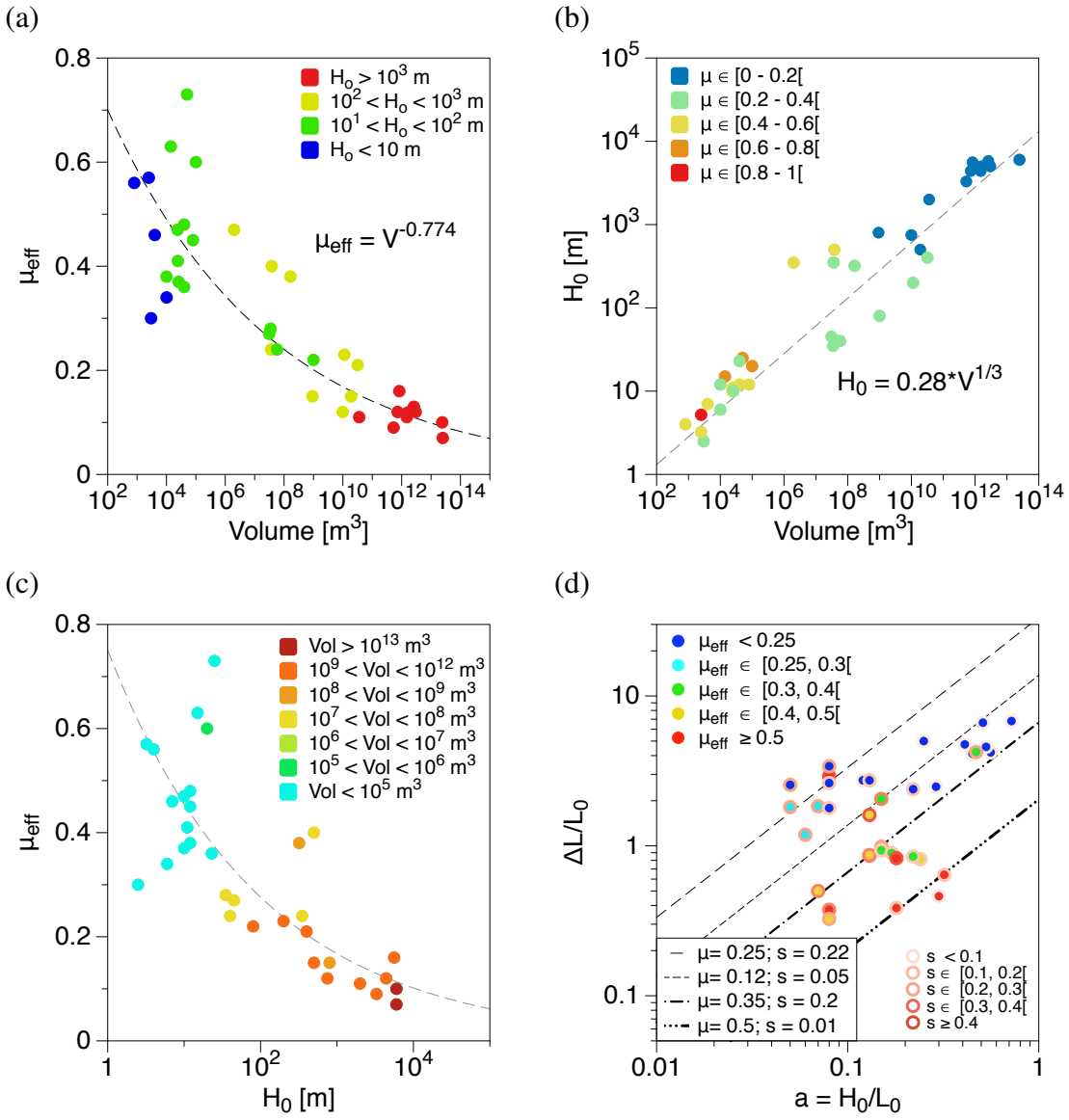

Supplementary Figure 5 **| Interdependence analysis for well constrained landslides on Earth, Mars, Io and Iapetus.** Each landslide is represented by a full circle. (a) Friction coefficient μ_{eff} as a function of the volume V, where the colour of each point represents the initial thickness of the released mass H_0. (b) Scaling law between the initial thickness H_0 and the volume V where the colour of each point represents the associated effective friction μ_{eff}. (c) Effective friction μ_{eff} as a function of the initial thickness H_0. (d) The normalized runout ($\Delta L/L_0$) as a function of the initial aspect ratio ($a = H_0/L_0$). Each circle represents a landslide where the colour inside the circle scales with μ_{eff} and the colour of its contour scales with the mean slope $s = \tan\theta$. The plain lines represent the theoretical curves calculated from supplementary equation (25) with some chosen values of $\mu = \tan\delta$ and $s = \tan\theta$. For the sake of clarity, error bars are not shown but are approximately twice the size of each symbol. Data from Supplementary Tab. 1.

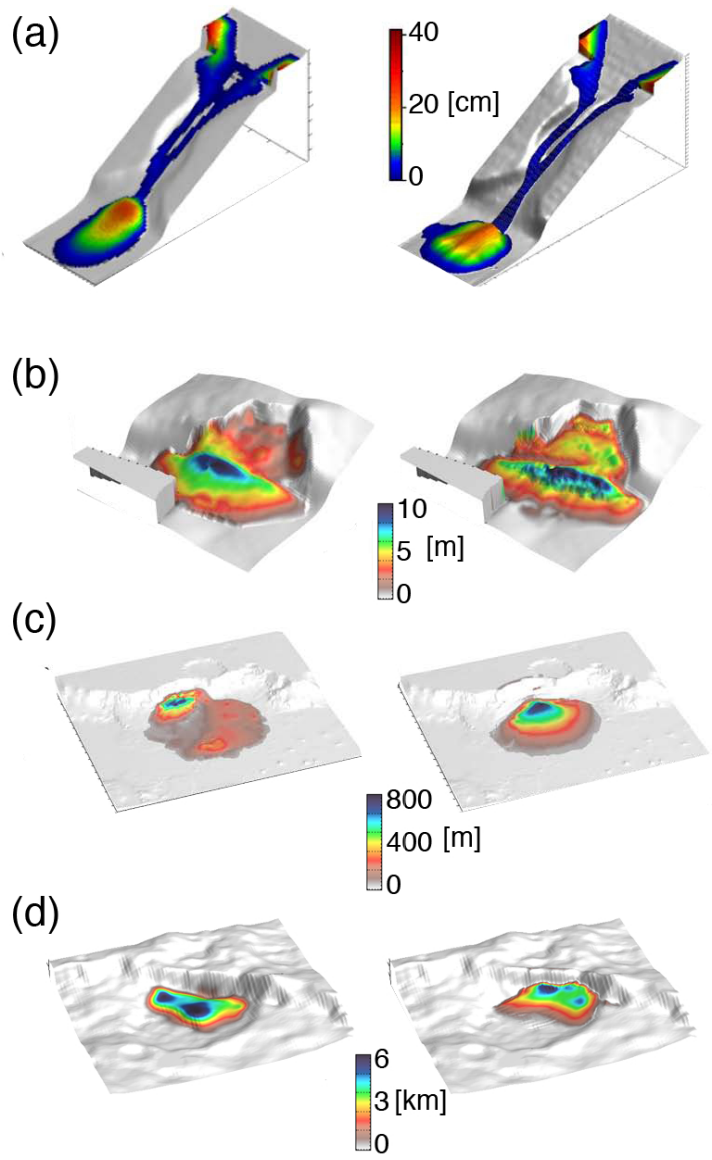

Supplementary Figure 6 **| Examples of numerical simulation of landslides with a constant friction coefficient μ_s over a wide range of volumes and planetary environments for which we have a DTM.** Observations are on the left column and simulations on the right column. (a) Experimental dry granular flows[2]. (b) Fei Tsui landslide in Hong Kong (c) Ganges Chasma landslides on Mars and (d) Malun Crater landslide on Iapetus.

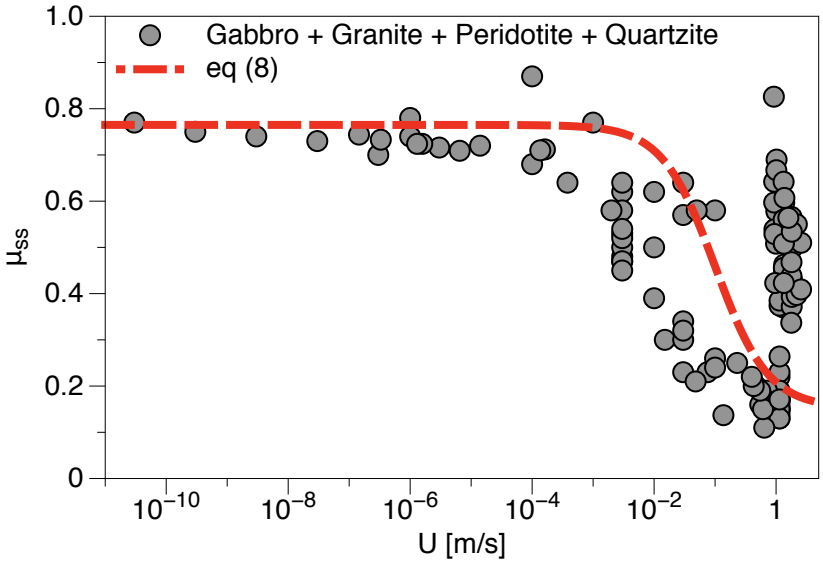

Supplementary Figure 7 | Steady-state friction coefficient μ_{ss} from rock friction laboratory experiments as a function of the slip rate. Summary of experiments involving only the igneous rocks reported[3]. The red curve is the best fit of equation (8), leading to $\mu_o = 0.76$, $\mu_w = 0.15$, and $U_w = 0.1$ ms^{-1}.

(a)

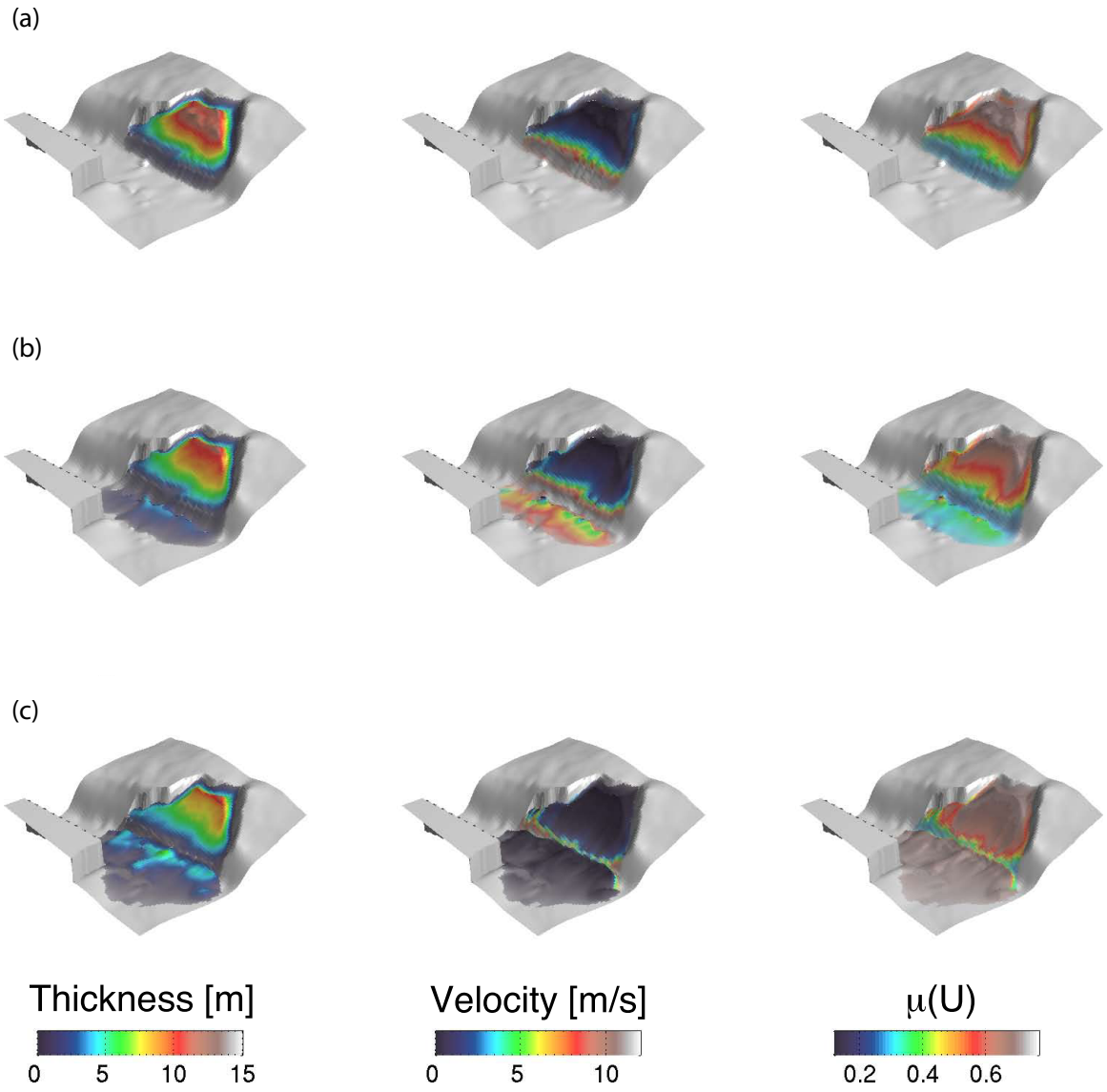

Supplementary Figure 8 **| Simulation of landslides over 3D topography, taking into account friction weakening.** The friction coefficient is derived from equation (3) with $\mu_o = 0.84$, $\mu_w = 0.11$, $U_w = 4.1$ ms^{-1}. Thickness, velocity and friction coefficient at three different times during the flow are shown for (a) Fei Tsui (Hong Kong) (b) Frank slide (Canada) and (c) Coprates (Mars).

(b)

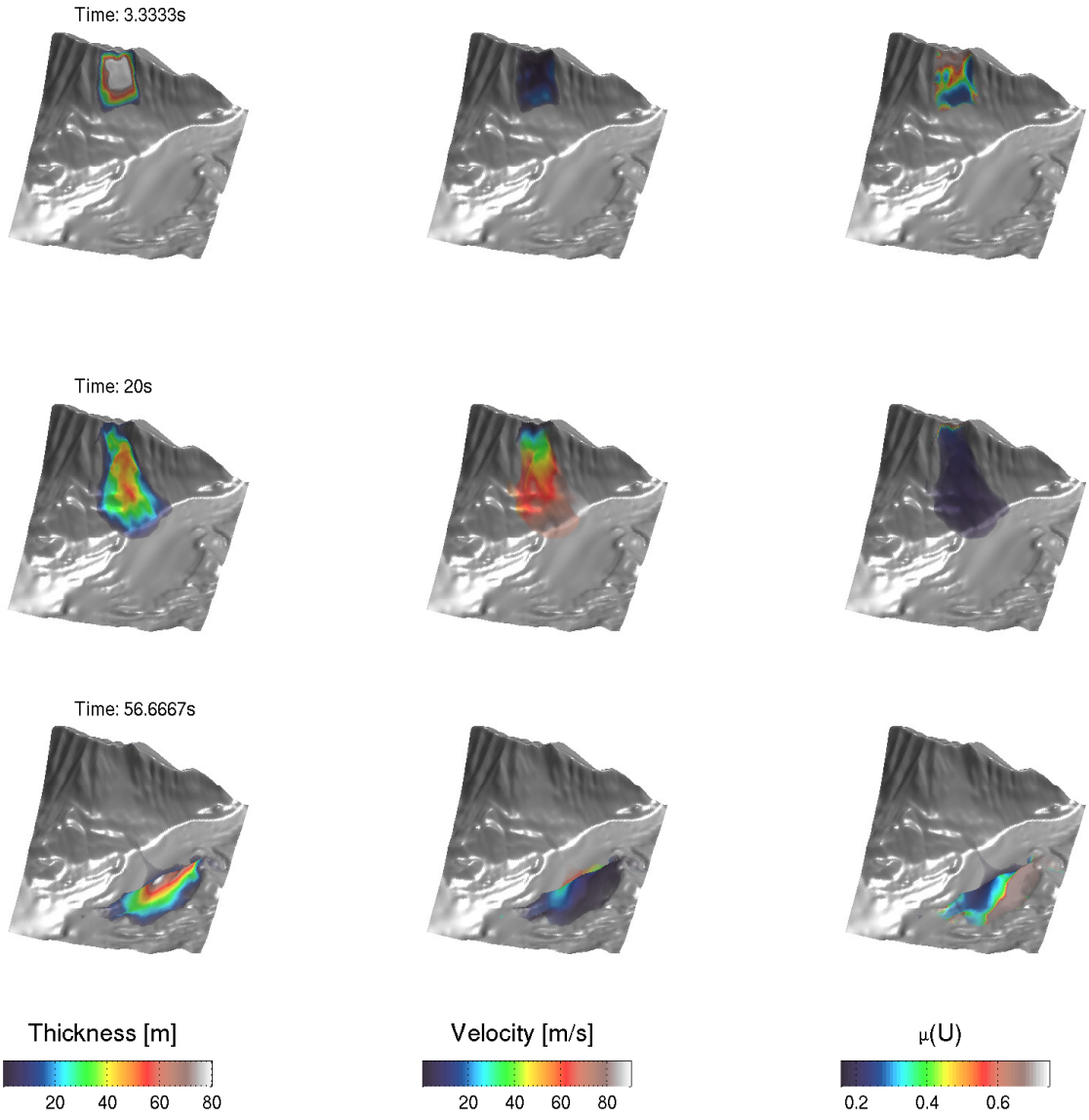

figure 8 continued

(c)

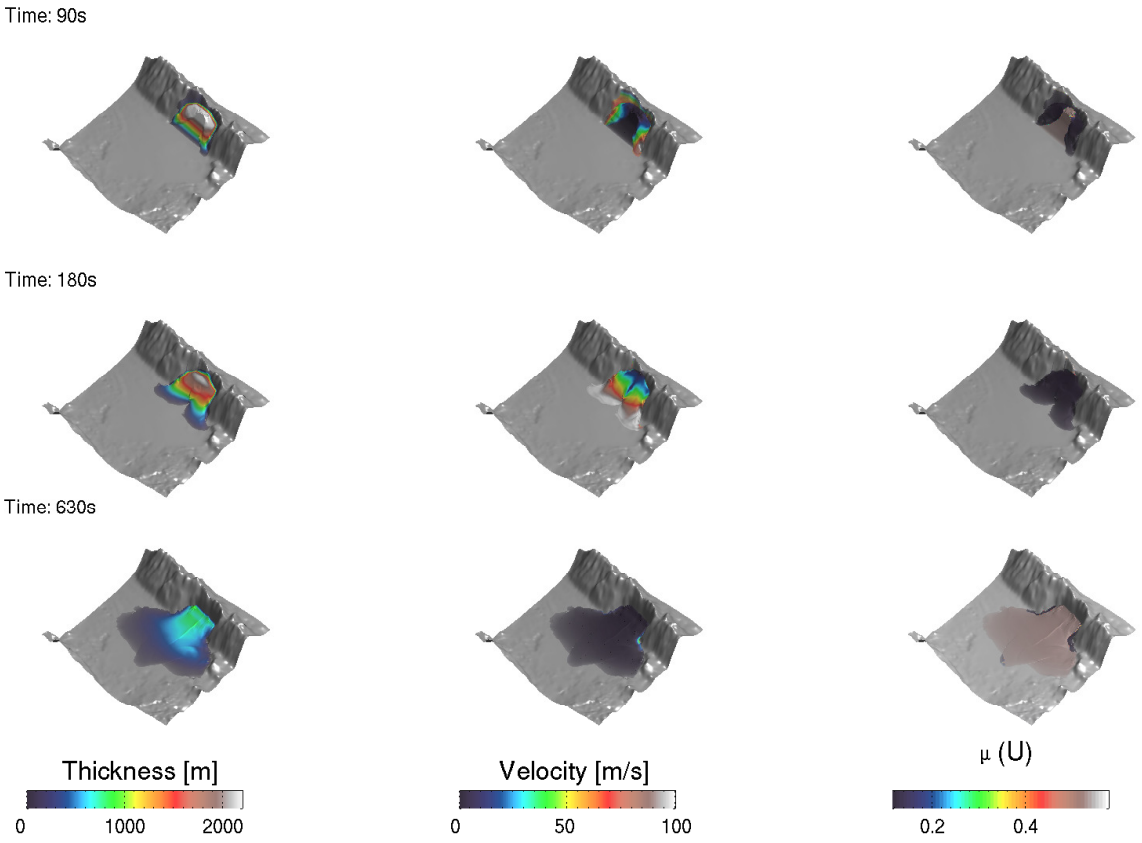

end of Supplementary Fig. 8

(a)

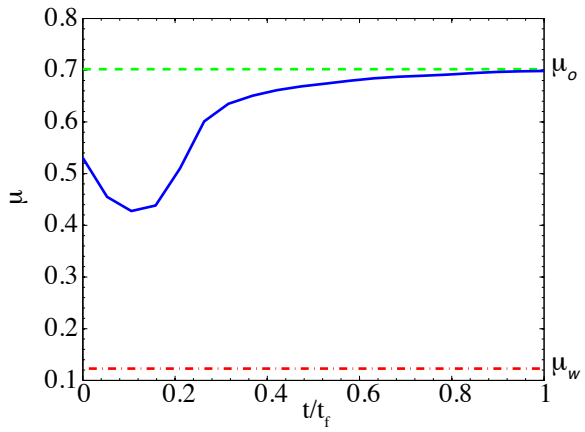

(b)

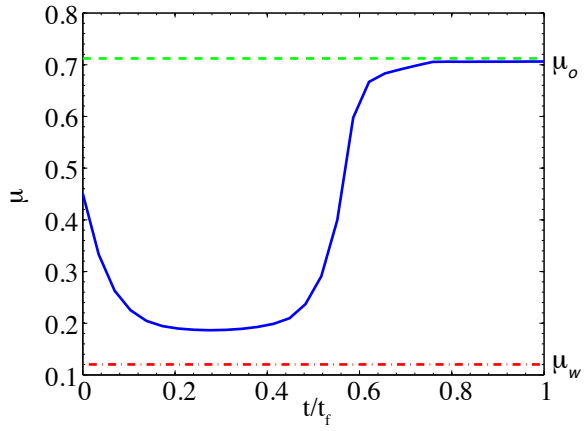

(c)

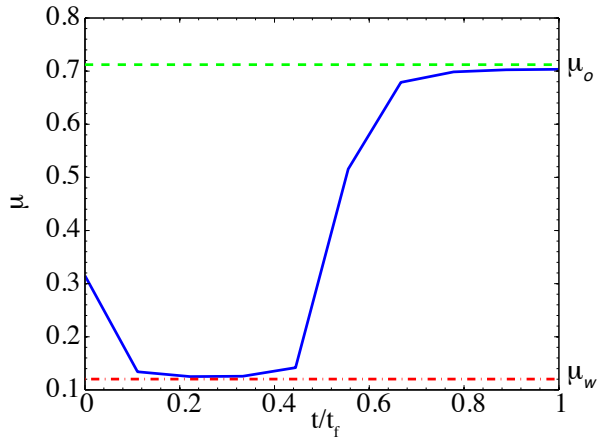

Supplementary Figure 9 **| Mean friction coefficient** $\mu(U)$ **in velocity-weakening simulations.** versus time. (a) Fei Tsui (b) Frank slide and (c) Coprates (see figure 5 and supplementary figure 8), when using the friction weakening law derived from flash heating concept (equation (3)) with $\mu_o = 0.84$, $\mu_w = 0.11$, $U_w = 4.1$ ms^{-1}.

Supplementary Table 1 | Landslide Summary Characteristics

Name	Vol. [m^3]	$H/\Delta L'$	$\Delta L'$ [m]	H_0 [m]	ΔL [m]	H_0/L_0	$\tan\theta$	μ_{eff}	Reference	Data Origin
Earth (g=9.81)										
Po Shan Road	4.00E+04	0.51	231.66	12	148.31	0.13	0.40	0.48	King (1999)	Field survey
Tsing Yi 1	2.40E+04	0.65	66.25	10	66.09	0.13	0.32	0.47	King (1999)	Field survey
Tsing Yi 2	4.00E+03	0.7	23.76	7	23.76	0.24	0.16	0.46	King (1999)	Field survey
Tuen Mun	8.00E+04	0.61	80.15	12	80.13	0.13	0.30	0.45	King (1999)	Field survey
Fei Tsui	1.40E+04	0.49	68.31	15	30.04	0.32	0.13	0.49	King (1999)	Field survey
Tin Wan	2.44E+04	0.58	72.75	11	72.43	0.15	0.26	0.41	King (1999)	Field survey
Island Road	8.00E+02	0.47	63.44	4	18.71	0.08	0.34	0.56	King (1999)	Field survey
Siu Sai Wan	1.01E+04	0.51	37.42	6	37.38	0.15	0.18	0.34	King (1999)	Field survey
Sham Shui Kok	4.00E+04	0.53	120.96	23	120.94	0.17	0.17	0.36	King (1999)	Field survey
Lai Ping Road	1.00E+05	0.38	142.84	20	42.77	0.18	0.13	0.60	King (1999)	Field survey
Ville de Cascade	1.00E+04	0.6	46.29	12	46.29	0.22	0.12	0.38	King (1999)	Field survey
Ching Cheung	3.00E+03	0.38	81.22	2.5	49.38	0.06	0.25	0.30	King (1999)	Field survey
Fei Ngo Shan	2.50E+03	0.58	170.61	3.23	117.9	0.08	0.55	0.57	King (1999)	Field survey
Shum wan	2.60E+04	0.41	137	10	137	0.15	0.31	0.37	King (1999)	Field survey
Frank slide	3.60E+07	0.20	3800	350	3800	0.22	0.18	0.24	Hungr (1981)	DTM + field survey
Thurwieser	2.00E+06	0.41	2500	350	2500	0.07	0.36	0.47	Sosio et al. (2008)	DTM + field survey
Valpola	3.80E+07	0.45	2035	500	2035	0.08	0.23	0.40	Crosta et al. (2007)	DTM + field survey
Socompa	3.60E+10	0.05	40000	2000	40000	0.25	0.07	0.11	Kelfoun & Druitt (2005)	DTM + field survey
Blackhawk	0.3E+09	0.09-0.13	9000	800	8000	?	0.08	0.15	Shreve (1987)	Field survey
St Helens	2.8E+09	0.09	23000	?	?	?	$\sim$0.08	$\sim$0.15	Voight et al. (1983)	Field survey
Montserrat	4.00E+07	0.25	3500	180	4500	0.26	0.18	0.23	Young et al. (1998)	Field survey
Mount Steller	6.00E+07	0.24	9120	135	$\sim$7000	0.08	0.11	0.22	Moretti et al. (2012)	Field survey
Dry Experiments	2.80E-03	0.35-0.49	0.47-1.87	0.14	0.27-1.17	0.7	0-0.44	0.50-0.53	Mangeney et al. (2010)	Experimental work
Dolomieu Crater flow	4.00E+02	0.71	420	20	407	0.2-0.3	$\sim$0.67	0.71	Hibert et al. (2011)	DTM + field survey
Mars (g=3.73)										
Ophir	8.33E+11	0.14	52000	5600	42020	0.56	0.030	0.16	Lucas et al., (2011)	DTM (PEDR MOLA)
Ophir West	1.50E+12	0.15	47000	4400	38000	0.53	0.001	0.11	Lucas et al., (2011)	DTM (PEDR MOLA)
Coprates	7.30E+11	0.08	62000	4400	51000	0.41	0.040	0.12	Lucas et al., (2011)	DTM (PEDR MOLA)
Ius	2.60E+12	0.12	66000	5800	53120	0.45	0.022	0.13	Lucas et al., (2011)	DTM (MeX/HRSC)
Ganges Landslide 1	5.30E+11	0.10	50000	3290	42800	0.51	0.020	0.09	Lucas et al., (2011)	DTM (PEDR MOLA)
Ganges Landslide 2	1.90E+10	0.13	22300	500	16410	0.08	0.120	0.15	This study	DTM (MRO/CTX)
Ganges Landslide 3	9.95E+09	0.14	22316	750	17125	0.12	0.080	0.12	This study	DTM (MeX/HRSC)
Olympus Mons	1.65E+08	0.40	3460	320	2879	0.47	0.270	0.38	This study	DTM (MRO/CTX)
Crater ManySlides 1	3.11E+07	0.24	1810	45	1182	0.07	0.240	0.27	This study	DTM (MRO/CTX)
Crater ManySlides 2	5.76E+07	0.23	2169	40	1699	0.08	0.220	0.24	This study	DTM (MRO/CTX)
Crater ManySlides 3	3.49E+07	0.30	1920	35	1271	0.05	0.258	0.28	This study	DTM (MRO/CTX)
Equatorial Crater	1.13E+10	0.13	4600	200	4468	0.08	0.190	0.23	This study	DTM (MeX/HRSC)
Shalbatana Vallis 1	3.19E+10	0.07	11500	400	8419	0.13	0.170	0.21	This study	DTM (MeX/HRSC)
Shalbatana Vallis 2	1.00E+09	0.20	5600	80	4082	0.05	0.210	0.22	This study	DTM (MeX/HRSC)
Iapetus (g=0.223)										
Malun	2.40E+13	0.123	65000	6000	56666	0.72	$\sim$0	0.1	This study[a]	DTM (Cassini/ISS)
Iapetus2	1.60E+12	0.118	80000	5000	76875	1.6	$\sim$0	0.119	Singer et al., (2012)	DTM (Cassini/ISS)
Iapetus3	3.00E+12	0.1333	60000	5000	42760	0.29	$\sim$0	0.12	Singer et al., (2012)	DTM (Cassini/ISS)
Io (g=1.796)										
Euboea Montes	2.50E+13	0.0846	125000	6000	81000	?	$\sim$0	0.07	This study[b]	DTM (Galileo/ISS)
Vesta (g=0.25)										
Landslide 1	4.5E+9 $\times \sum H^c$	0.2-0.3	45000	?	29000	?	$\sim$0	?	This study	DTM (Dawn/FC)
Landslide 2	6.8E+9 $\times \sum H^c$	0.2-0.3	68800	?	48000	?	$\sim$0	?	This study	DTM (Dawn/FC)
Landslide 3	4.7E+9 $\times \sum H^c$	0.2-0.3	58000	?	24000	?	$\sim$0	?	This study	DTM (Dawn/FC)

[a]A different volume has been found for this landslide[7], but we completely reconstruct the landslide and thus use our calculation. [b]Previously analyzed[8] but the data are not accessible.[c]The Dawn mission offers stereo over Vesta's landslides[9]. We built the DTMs but they cannot resolve accurately the deposits in height. Therefore, only the area of the deposits are presented, but in order to estimate the volume this value need to be multiplied by the integral thickness $\sum H$. These values are shown here only for comparison but are not discussed in the main text. Topography for landslides on the Moon, Venus, Callisto and Rhea could not be derived as the resolution or the coverage of the current data does not allow deposit analysis. References listed in the table correspond to cited studies[4–7, 10–18] and references therein. Locations of Martian landslides are shown in supplementary figure 3.

Supplementary Table 2 | Weakening Model Parameters for Landslide Characteristics

	Earth			Mars		Iapetus
Models Considered	Soil	Rock	LR Rock	LR Rock	LR Ice-Rock Mix	LR Ice
Gravity [m/s^2]	9.81	9.81	9.81	3.73	3.73	0.224
Maximum Velocity^a, U_{max} [m/s]	12	60	90	132	132	56
Median Velocity^a, U_{Q50} [m/s]	0.5 - 10	5 - 15	10 - 20	15 - 30	15 - 30	15
Mean Velocity^a, $\bar{U}$ [m/s]	2 - 10	8 - 15	20 - 50	10 - 20	10 - 20	10
Normal Stress^a, σ_n [MPa]	0.43	1.24	69	49	35	2.93
Contact Shear Strength^b, τ_c [MPa]	10 - 30	800 - 1200	1500 - 3000	3000	3000	250 - 650
Thermal Diffusivity^c,α_{th} [mm^2/s]	0.18	1.4	1.4	1.4	0.7	1.18
Heat capacity^c, ρc [MPa/K]	1.4	2.7	2.7	2.7	2.2	1.3
Temperature rise^d, $\Delta T = T_w - T$ [K]	900	900	900	906	925	150
Friction coefficient^a, μ_{eff}	0.49	0.43	0.11	0.115	0.115	0.12
Sliding distance of asperity contact^c, D_a [μm]	0.5 - 100	0.5 - 100	0.5 - 100	0.5 - 100	0.5 - 100	0.5 - 100
Runout distance^a, ΔL [m]	30	2000	50 x 10^3	52 x 10^3	52 x 10^3	65 x 10^3
Weakening sliding Velocity, U_w [m/s]	3 - 5700	0.05 - 26	0.01 - 8	0.01- 2	0.003 - 0.7	0.001 - 1.5

^{a} values obtained from our simulations. ^{b}The contact shear strength τ_c is estimated from the shear wave velocity in different materials and gives a possible range for landslide application. ^{c}Values taken from previous work[19] and references therein and adapted for landslide application. $^d\Delta T$ is estimated for a given initial depth and a simplistic estimate of geothermal heat for each of the planets. We typically used 10.6 K/km for dry zones and 6.4 K/km for ice-saturated zones on Mars. No geothermal heat is assumed for Iapetus which probably leads to an overestimation of ΔT as all Iapetian landslides are deep-seated. T_w for rocks are taken from previous work[19] and references therein. For rock-ice and ice, values have been estimated to within an order of magnitude. ^{e} The mean velocity $\bar{U}$ has been used. The sliding velocity weakening has been estimated using a sliding distance of asperity contact D_a with a range of three orders of magnitude.

Supplementary Table 3 **| Variables list**

Variable Name	Description and units
α_{th}	Thermal diffusivity [mm^2/s]
$\dot{\gamma}$	Shear rate [s^{-1}]
d	grain diameter [mm]
D_a	Sliding distance of asperity contact [μm]
δ	Friction angle (= atan(μ)) [^{o}]
ΔL	Front travel distance [m] (*see Supplementary Fig. 1*)
$\Delta L'$	Maximum distance travelled [m] (*see Supplementary Fig. 1*)
$\Delta T = T_w - T$	Temperature rise [K]
θ	Mean slope of the bottom topography [^{o}] (*see Supplementary Fig. 1*)
g	Acceleration due to gravity [m/s^2]
H	Total fall height [m] (*see Supplementary Fig. 1*)
H_0	Initial height [m] (*see Supplementary Fig. 1*)
I	Inertial number [*]
I_0	characteristic inertial number [*]
L_0	Initial length [m]
μ	friction coefficient [*]
μ_{eff}	effective friction coefficient [*]
μ_w	Weakening friction coefficient [*]
ρ_s	Solid density [kg/m^3]
ρc	Heat capacity [MPa/K]
σ_n	Normal Stress [MPa]
τ	Shear stress [MPa]
τ_c	Contact Shear Strength [MPa]
$\bar{U}$	Mean Velocity [m/s]
U_{max}	Maximum Velocity [m/s]
U_{Q50}	Median Velocity [m/s]
U_w	Weakening sliding Velocity [m/s]

Supplementary Table 4 | Regression Statistics

Metrics	$f(x)$	R^2	σ	s
$H/\Delta L'$ vs V	$1.2 \times V^{-0.089}$	0.765	0.10605	0.10747
$\Delta L'$ vs V (a)	$6.01 \times V^{-0.371}$	0.918	0.14164	0.14266
$\Delta L'$ vs V (b)	$3.23 \times V^{-0.354}$	0.956	0.25778	0.26115
H_G/L_G vs V	$V^{-0.0459}$	0.791	0.071	0.075
μ_s vs μ_{eff}	$\mu_s = \mu_{eff}$	0.966	0.0237	0.0248
μ_{eff} vs V	$V^{-0.0774}$	0.84	0.0667	0.0675
μ_{eff} vs U (c)	$5.3 \times U^{-0.87}$	0.934	0.050	0.0545
H_0 vs V	$1.86 \times V^{0.28}$	0.974	228.3	232.2
L_0 vs V	$7.5 \times V^{0.397}$	0.985	411.35	418.15

R^2 is the coefficient of determination, σ the standard deviation and s the sample standard deviation. [a]Fit obtained using data from literrature[20]. [b]Best fit obtained with our datasets (see table 1). [c]Maximum velocity values obtained in our terrestrial simulations.

Supplementary Note 1
Analysis and limitations of the landslide data sets

Landslide data are frequently analysed using simple considerations on the energy balance between their initial and final states. For the simple case of a rigid block sliding over a rigid topography, the loss of potential energy between the initial released mass and the final deposit is equal to the work of the resisting force over the total sliding distance of the block. If the resisting force is governed by Coulomb friction with constant friction coefficient, this energy balance gives[21,22]

$$MgH_G = \mu MgL_G, \tag{1}$$

where g is acceleration due to gravity, M the mass, μ the friction coefficient between the block and the bed, H_G the falling height of the centre of mass of the block and L_G its travel distance in the horizontal direction. Supplementary equation (1) leads to the following relationship between the friction coefficient and the characteristic lengths of the block trajectory:

$$\frac{H_G}{L_G} = \mu. \tag{2}$$

Note that this relationship does not depend on gravity or mass. The common idea is to use this relationship for a landslide even though its real energy balance is different from that of a sliding block. As H_G and L_G are very difficult to measure in the field, it has been proposed[21] to replace these quantities by the difference in height H and in horizontal distance $\Delta L'$ between the maximum elevation point of the initial mass and the minimum elevation point of the deposit (see supplementary figure 1). For this reason, studies often consider the so-called Heim's ratio $H/\Delta L'$, and interpret it as an effective friction coefficient μ_{eff}, assumed to be characteristic of the mean dissipation forces at work during the flow[20] (see supplementary figure 2).

Figure 2-a reports the Heim's ratio as a function of landslide volume, inferred from a compilation of terrestrial and planetary data extracted from the literature and new data from Digital Topography Models (DTM) we built and/or from very accurate field observations[10,11]. These high quality data are represented by symbols with thick black contours. These data consist of measurements of the maximum runout distance $\Delta L'$ and of the total falling height H as defined in supplementary figure 1 for several geometries. These two parameters can be easily estimated from field studies and from aerial/satellite imagery analysis. A more difficult measurement is the landslide volume. The volume can be recovered by image processing when the initial scar is not covered by the deposits or from the difference between pre and post-event Digital Topography Models as previously discussed[12] for Martian landslides. Note that a variation of up to 20% between the initial released mass and the final deposit can be observed due to dilatancy effects[11,12,23].

In the literature, measurements of Terrestrial landslide characteristics (volume, initial shape of the released mass, underlying topography, etc.) are not always available, in particular due to post-event weathering processes that overprint critical information. Paradoxically, more data can be sometime recovered remotely for landslides on planetary bodies such as Mars, because of their lower erosion rate, the absence of vegetation and free access to satellite imagery data from planetary missions (*e.g.* Magellan, Lunar Reconnaissance Orbiter, Mars Express, Mars Reconnaissance Orbiter, Cassini/Huygens and Galileo).

For more than forty landslides, we were able to derive a DTM or had access to high quality data from detailed field surveys (symbols with thick black contours in figure 2-a and supplementary table 1). However, for most of the planetary landslides other than Martian landslides, volume measurements were not possible due to the absence of an accurate DTM. This is the case for the selected landslides on the Moon, Venus and on Icy Moons represented in figure 2. For these landslides, the volume was roughly deduced from the measurement of $\Delta L'$ using the empirical scaling law observed for Terrestrial events for which $\Delta L'$ and V are

known, as done or suggested by previous studies[7,24,25]. When using the well constrained data for which we have a DTM or precise field data (see inset in figure 2-a), we find:

$$\Delta L' = 3.2 \times V^{0.35}. \tag{3}$$

Note that the best fit to the Terrestrial data[20] (blue circles of figure 2-a) gives $\Delta L' = 6 \times V^{0.37}$. The origin of this scaling law, essentially related to geometrical effects, is discussed here, based on an analytic solution for granular flows (see supplementary equations (22)–(24)). When plotted in figure 2-a, these landslides follow a trend similar to the better constrained Terrestrial and Martian data (Figure 2). However, we did not include these low accuracy data in the following.

Except for the previous data on Martian landslides[26], all the data, including our Martian landslides, follow a similar trend, clearly showing a decrease of the Heim's ratio when the volume increases (Figure 2-a,b), whatever the gravitational acceleration, the material involved or the physical processes specific to the different environments.

For Martian landslides within the Valles Marineris area, a large morpho-tectonic complex near the equator with troughs of almost 5 km depth, there is indeed a strong discrepancy between our dataset obtained from satellite imagery and that reported previously[26] (respectively orange squares and pink squares in figure 2-a). The difference between these two datasets is mainly related to their origin. Actually, the previous study[26] used the gridded MOLA (Mars Orbiter Laser Altimeter) data providing a 463 m/post interpolated DTM from the individual Precision Experiment Data Records (PEDRs) altimetry profiles. This was the best dataset available at the time of their study. Our volume calculation was based on DTMs that we derived from stereo pairs of CTX (Context Camera) images more recently collected by the Mars Reconnaissance Orbiter mission. This provides a spatial sampling of $\sim$5 m/pixel and therefore $\sim$25 m/post for the altimetry grid[27]. When no CTX stereo pairs were available, we used HRSC (High Resolution Stereo Camera) images that can provide DTMs with 50-100 m/post of resolution[28]. Our DTMs can resolve smaller landslides than the ones identified previously[26], leading to wider range of volumes. Furthermore, while they[26] have carried out a very large inventory of Martian landslides (*i.e.* the largest to date), we have only selected here landslides that were free to flow, *i.e.* those that were not stopped by the opposite walls as this is mostly the case in the Valles Marineris system (the locations of our examples is shown in supplementary figure 3). Unfortunately, most of these large landslides were actually stopped[26]. As a result, their values of $H/\Delta L'$ ratio are systematically greater than ours, a point that has been already discussed[29].

In order to quantify the decrease of the Heim's ratio with volume, we only consider the data subset for which DTM and/or field survey investigations provide accurate volume estimates and associated uncertainties (symbols with thick black contours in figure 2-a). The best fit of these selected data gives the following empirical relationship (Figure 2-a):

$$\frac{H}{\Delta L'} = 1.2 \times \frac{1}{V^{0.089}}. \tag{4}$$

For the data subset where DTMs are available, we can estimate the ratio between the elevation drop and the travel distance of the centre of mass, *i.e.* H_G/L_G. Supplementary figure 2 shows that this ratio also decreases with the volume, as already shown previously[4], in a very similar way as the Heim's ratio:

$$\frac{H_G}{L_G} = \frac{1}{V^{0.0859}}. \tag{5}$$

Supplementary Note 2
Analytical formulation of the effective friction

Analytical development

Following former studies of our group[16,18,30], we use the analytical solution developed previously[31–33] that describes the collapse over an inclined plane of angle θ of a granular mass of effective friction coefficient $\mu_{eff} = \tan\delta$, where δ is the effective friction angle of the granular material. This solution is derived from the 1D thin-layer depth-averaged equations of mass and momentum conservation with a Coulomb friction law, using the method of characteristics (see previous works[31,33] for more details). The friction coefficient formally appears in the basal friction force in the momentum equations. However, once fitted to reproduce specific experiments or natural landslides, this friction coefficient can be interpreted as an empirical friction coefficient that describes the mean dissipation during the flow, including the dissipation within the bulk (*e.g.* see previous study[34]). Note that the thin-layer depth-averaged models give reasonable estimates of granular flow deposits for initial aspect ratios smaller than one, which is the case for all the natural events considered here, as listed in table 1 (refer to the previous study[35] for discussion).

The analytical solution of the one-dimensional dam-break problem over inclined planes[31] provides the evolution of the mass profile and therefore of the front with time (see equation (21) in 31 and the following text as well as case 1.1 of section 3.1 in 33). The front position x_f (called x_L on p. 1086 of 31) is given by

$$x_f(t) = 2t\sqrt{kgH_0\cos\theta} - \frac{g}{2}\cos\theta(\tan\delta - \tan\theta)t^2. \tag{6}$$

where k is considered here to be an empirical coefficient (see p. 1086 of 31 and 32 for more details) and H_0 is the initial thickness of the released mass. The front velocity then reads:

$$v_f(t) = 2\sqrt{kgH_0\cos\theta} - g\cos\theta(\tan\delta - \tan\theta)t. \tag{7}$$

The front stops when the velocity vanishes ($v_f = 0$) at time:

$$t_f = \sqrt{\frac{kH_0}{g\cos\theta}}\frac{2}{\tan\delta - \tan\theta}. \tag{8}$$

Replacing t in (6) by t_f from (8) gives $\Delta L = x_f(t_f)$:

$$\Delta L = \frac{2kH_0}{\tan\delta - \tan\theta}. \tag{9}$$

Supplementary equation (9) with an empirical coefficient $k = 0.5$ reproduces quantitatively the results of experiments of granular collapse over horizontal and inclined beds, in particular the dependence of ΔL on inclination angle, on initial aspect ratio and on initial thickness of the released mass[16,35]. We hence set $k = 0.5$ and adopt here the following semi-empirical relationship:

$$\Delta L = \frac{H_0}{\tan\delta - \tan\theta}. \tag{10}$$

The effective friction coefficient $\mu_{eff} = \tan\delta$ can be simply derived from supplementary equation (10) as:

$$\mu_{eff} = \tan\theta + \frac{H_0}{\Delta L}. \tag{11}$$

According to supplementary equation (11), the effective friction coefficient μ_{eff} can be retrieved from field

measurements of the initial thickness of the released mass H_0, the downslope runout distance ΔL and the mean slope angle along the landslide path θ.

Now, let us calculate the Heim's ratio $H/\Delta L'$. From supplementary figure 1 we obtain:

$$H = H' + H", \tag{12}$$

with

$$H" = \frac{H_0}{\cos\theta}, \tag{13}$$

and

$$\tan\theta = \frac{H'}{\Delta L'}. \tag{14}$$

Combining these relationships gives:

$$\frac{H}{\Delta L'} = \tan\theta + \frac{H_0}{\Delta L' \cos\theta}. \tag{15}$$

Noting that

$$\Delta L' = (\Delta L + L_0)\cos\theta - H_0 \sin\theta, \tag{16}$$

supplementary equation (15) gives

$$\frac{H}{\Delta L'} = \tan\theta + \frac{H_0}{\cos^2\theta\,(\Delta L + L_0 - H_0\tan\theta)}. \tag{17}$$

If we replace (9) in (17) the Heim's ratio reads:

$$\frac{H}{\Delta L'} = \tan\theta + \frac{1}{\cos^2\theta\left(\frac{2k}{\tan\delta - \tan\theta} + \frac{L_0}{H_0} - \tan\theta\right)}. \tag{18}$$

Supplementary equation (18) shows that $H/\Delta L'$ depends on the slope of the topography, the aspect ratio $a = H_0/L_0$ and the effective friction $\tan\delta$.

Supplementary equations (11) and (18) show that the Heim's ratio $H/\Delta L'$ is generally not equal to the effective friction. Indeed, only the first term in these two equations, $\tan\theta$, is the same. This first term corresponds to H_G/L_G for a block sliding over an inclined plane. Note that for a block sliding over a curved topography, from steep to gentle slopes, the mean slope experienced by its centre of mass depends indirectly on the friction coefficient. Indeed, for high friction the block will stop on high slopes, while it will reach gentler slopes for smaller friction. For a mass spreading over such a curved topography, the mean slope calculated along the path of the avalanche front will be smaller than H_G/L_G, because the front is located downslope compared to the centre of mass. The second terms of supplementary equations (11) and (18) take into account the spreading of the mass over the topography. Consequently, the two regimes (*i.e.* sliding and spreading) described in 36 are clearly identified here. While the expression of the second term is very simple for the effective friction (supplementary equation (11)), for the Heim's ratio (supplementary equation (18)) it results from a complex interplay between different quantities.

Application to real data

We estimate μ_{eff} for the well constrained data presented previously by replacing the parameters in supplementary equation (11) by the measurements on real landslides. The mean slope for natural landslides is taken as the slope averaged along the path travelled by the landslide front. Figure 3-a compares μ_{eff} to

$H/\Delta L'$, and shows that the two quantities are almost equal for small values, while they differ significantly for larger values. In other words, $H/\Delta L' \simeq \mu_{eff}$ for landslides with large volumes, whereas they are different for small volumes, typically $V < 10^6$ m^3. For example, while $H/\Delta L' = 0.7$ and $\mu_{eff} = 0.46$ for the Tsin Yi 2 landslide ($V = 4 \times 10^3$ m^3), we find $H/\Delta L' \simeq \mu_{eff} \in [0.11 - 0.15]$ for the Martian Ophir West landslide ($V = 1.5 \times 10^{12}$ m^3). For very large volumes, $V > 10^8$ m^3, the Heim's ratio is equal to or overestimates the effective friction. Figure 2-c shows that the effective friction μ_{eff} decreases with increasing volume for natural landslides. For small volumes $V < 1000$ m^3, the friction coefficient is about 0.7, and it reduces to $\mu_{eff} < 0.1$ for $V > 10^{10}$ m^3 following the empirical relationship (see Supplementary Fig. 5-a)

$$\mu_{eff} = \frac{1}{V^{0.0774}}. \tag{19}$$

While a similar trend is observed for the Heim's ratio $H/\Delta L'$ (supplementary equation (4), Figures 2-b,c, 4-b and 5-a), the use of μ_{eff} instead of $H/\Delta L'$ significantly reduces the scatter in the data (see Table 4), especially for small and intermediate volumes (Figure 2-b,c). Interestingly, the observed trend of $\mu_{eff}(V)$ is closer to $H_G/L_G(V)$ (supplementary equation (5)) than to $H/\Delta L'(V)$ (supplementary equation (4)). Note that if we include the results from granular flow experiments (glass beads), the dataset as a whole is consistent with saturation of the friction coefficient at small volumes approaching a value typical of the material involved (0.6 for glass beads, 0.7 for rocks). Indeed, for laboratory experiments, μ_{eff} has been shown to be approximately constant[16,37]. However, the small range of volumes investigated in laboratory experiments makes it difficult to verify the weak volume dependence suggested by supplementary equation (19).

Interestingly, the main trends of $H/\Delta L'$ and μ_{eff} as a function of volume result from significant contributions of both the first and second terms of supplementary equations (11) and (18), respectively (Supplementary Fig. 4). For instance, for the Lai Ping Road landslide ($V = 1 \times 10^5$ m^3), the effective friction is $\mu_{eff} = 0.60$, while $\tan\theta = 0.13$ and $H_0/\Delta L = 0.46$. Whatever the volume, the two terms are of the same order of magnitude. More precisely, for small volumes, the first term is higher than the second term and they are equal at about $V = 10^6$ m^3 and $V = 5 \times 10^7$ m^3, respectively, for $H/\Delta L'$ and for μ_{eff} (Supplementary Fig. 4).

An important observation is that the mean slope angle globally decreases as the landslide volume increases (Supplementary Fig. 4-a). While small landslides can be observed on a very large range of slopes, from gentle to steep (up to $\tan\theta \simeq 0.6$), large landslides are only observed on gentle slopes ($\tan\theta$ smaller than 0.1). This is probably related to the limited characteristic length of relief variation. For large landslides (larger than 10^6 m^3), the mean slope on which they deposited provides a first estimate of the effective friction coefficient (see supplementary equation (11)). Supplementary figure 5 shows the dependencies among all variables (μ_{eff}, V, H_0 and L_0). As shown above, μ_{eff} decreases as the volume increases. As the volume is a function of the initial thickness H_0, μ_{eff} also decreases with increasing H_0 (Supplementary Fig. 5-a-c).

Finally, the analytical solution can be used to investigate the origin of the scaling law between $\Delta L'$ and V. Assuming that V is proportional to H_0^3, our well constrained natural data (Supplementary Fig. 5-b) results in

$$H_0 = \alpha \times V^{1/3}. \tag{20}$$

with $\alpha = 0.28$ (relaxing this assumption gives $H_0 = 0.45 \times V^{0.32}$).

Supplementary equation (10) then implies that the runout distance along the slope is

$$\Delta L = \frac{\alpha}{\tan\delta - \tan\theta} V^{1/3}. \tag{21}$$

Supplementary figure 1-b shows that $\Delta L' = (\Delta L + L_0 - H_0 \sin\theta)\cos\theta$, so that

$$\Delta L' = \left[\frac{\alpha \cos\theta}{\tan\delta - \tan\theta} V^{1/3} + L_0 - H_0 \sin\theta \right]. \quad (22)$$

In the data set considered here, $L_0 - H_0 \sin\theta << \Delta L'$, so that supplementary equation (22) reduces to

$$\Delta L' \simeq \beta V^{0.33}, \quad (23)$$

where

$$\beta = \frac{\alpha \cos\theta}{\tan\delta - \tan\theta}. \quad (24)$$

As a result, the dependence of μ_{eff} on the volume is expected to manifest itself in the pre-factor β and not in the exponent of the scaling law which seems to simply arise from geometrical considerations. This implies that recovering the geometrical scaling in the empirical relationships between $\Delta L'$ and V does not cast doubt on the dependence of the effective friction on the volume, which contradicts what was advanced by 38 and 36. From supplementary equation (11), we have $\frac{1}{\tan\delta - \tan\theta} = \frac{\Delta L}{H_0}$. Our data set shows that $1.7 < \Delta L/H_0 < 54$. For natural data $0° < \theta < 30°$, so that $0.87 < \cos\theta < 1$. For $\alpha = 0.28$, this gives approximately $0.5 < \beta < 15$. Hence, the analytical solution predicts the same form of the scaling law for large and small volumes (*i.e.* $\Delta L' \propto V^{0.33}$) but with a smaller pre-factor for smaller volumes. This is in good agreement with natural observations, which in an overall manner follow supplementary equation (3), implying $\beta = 3.2$ and a volume dependence on $V^{0.35}$. Fitting small and large landslides separately, we find $\beta \simeq 10$ for $V < 10^6$ m^3 and $\beta \simeq 20$ for $V > 10^8$ m^3, with only slightly different volume dependencies (see inset in Figure 2-a).

Note that numerical simulations[12] show that for a given H_0, the shape of the initial scar affects the volume of the released mass but only weakly affects the runout distance $\Delta L'$. As a result, variability in the shape of the initial scar can affect the function $\Delta L'(V)$ and generate some scatter in the data. Nevertheless, the empirical relationship $\Delta L'(V)$ for our well constrained data set shows a good coefficient of correlation, $R^2 \simeq 0.956$ (table 4).

As discussed in 30, 32, 35, and 29, supplementary equation (9) gives

$$\frac{\Delta L}{L_0} = \frac{a}{\tan\delta - \tan\theta}, \quad (25)$$

where $a = H_0/L_0$ is the initial aspect ratio. This relationship fits granular collapse experiments well[16,29,39,40]. Consequently, natural landslide runout distances are well reproduced by supplementary equation (25) for typical values of μ_{eff} calculated from supplementary equation (11) and θ (Supplementary Fig. 5-d). However, the initial aspect ratio is not clearly defined if the initial scar and the morphology of the released mass are complex.

Supplementary Discussion
Potential mechanisms at the origin of the frictional weakening

The idea that reduced apparent friction could explain the high mobility of large landslides is not new. Several mechanisms have been proposed, such as lubrication by water or air, thermal pressurization, fragmentation, acoustic fluidization, flash heating or erosion[7,13,16,20,38,41–51]. Based on discrete elements simulations with varying particle size, 52 found significant shearing of the flowing mass and postulated that the apparent friction coefficient is proportional to the shear strain rate. While erosion processes may explain the increase of mobility for landslides over steep or moderate slopes,[47] laboratory experiments show that the erosion efficiency decreases as the slope decreases[16,53] and hence large landslides flowing over slopes of only a few degrees, such as the Valles Marineris landslides on Mars or the Socompa debris avalanche in Chile,

would hardly be affected by erosion processes unless they are fluidized[54]. Airless environments on the Moon, small asteroids like Vesta or on icy satellites like Iapetus rule out the air lubrication hypothesis as a unifying mechanism. Fluidization during the spreading phase, an idea recently re-visited[51], requires a fluid or a gas to permeate through the granular material and is unlikely in airless environments. While free water may be absent in some planetary environments, the fragmentation of particles may release water during the spreading phase. Evidence for this mechanism of decomposition has been found in field studies[55] and in laboratory experiments[56,57], indicating that weakening during slip may be due to several factors, but the most important is probably chemical pressurization, i.e. the dramatic increase of fluid pressure during a chemical reaction[58]. Acoustic fluidization could occur in vacuum environments and is a good candidate for explaining long-runout landslides throughout the Solar System. Unfortunately, this hypothesis is difficult to test in natural cases, even on Earth.

The type of velocity-weakening friction law derived from the flash heating mechanism makes it possible to reproduce the behaviour of a large range of landslides (equations (3) and (4)) as shown in the main text. Even though another mechanism could be at the origin of similar friction laws, flash heating seems to be one of the possible mechanisms. Indeed, as stated in a recent study[49] and references therein, deformation in landslides and other granular flows could be localized. Laboratory observations of velocity-weakening have been previously interpreted within the framework of flash heating for both rock sliding[59,60] and granular flows[61]. Note that velocity-weakening has been also observed for water ice[62], which is relevant for icy ground observed on the moons of giant planets such as Iapetus or Callisto where numerous landslides are observed. The friction derived from flash heating involves a characteristic velocity for the onset of weakening U_w. This velocity, controlled by competition between frictional heating and heat conduction, is defined[19] as :

$$U_w = \frac{\alpha_{th}}{D_a}\left(\frac{\rho c \Delta T}{\tau_c}\right)^2, \tag{26}$$

where α_{th} is the thermal diffusivity, D_a a characteristic micro-contact size, c the heat capacity, ρ the density, τ_c the local yield strength under shear loading and ΔT the difference between the initial temperature and the temperature at the onset of thermal weakening of the micro-contact. Realistic values of the weakening velocity for landslides (supplementary equation (26)) are proposed in supplementary table 2. The complexity of natural flows leads to a very large range for the possible values of the parameters involved in the friction law (equations (3) and (4)), in particular of U_w. Here we determine the empirical parameters that best fit the relationship between the effective friction and the velocity obtained with our constant-friction simulations (Figure 4-b). We find $\mu_o = 0.75$, $\mu_w = 0.08$ and $U_w = 4$ ms^{-1}. Note that U_w is in the range of the weakening velocities estimated for landslides (Supplementaty Tab. 2). Examples of simulations of real landslides taking into account the velocity-weakening friction law (3)-(4) with these parameters are given in supplementary figure 8 and 9. These figures show the variation of the friction coefficient for the different landslides, which can reach values as small as $\mu = 0.1$ during the first part of the flow and values as small as $\mu = 0.7$ during the decelerating phase. Note that the friction at the very beginning of the flow is quite high ($0.3 < \mu < 0.5$). The value of U_w fitted from our simulations is one order of magnitude larger than the value estimated[19] or by fitting the sliding friction experiments[3] (Supplementary Fig. 7). One possible explanation is that, in our case, the velocity U_w corresponds to the averaged velocity of the granular layer. However, in granular flows, the velocity varies on a thickness of several grains: granular flow experiments show almost linear or Bagnold velocity profiles but strain localisation near the bottom is expected to occur in natural flows. If we assume that the velocity varies on a layer larger than ten grains (which is a characteristic correlation length in granular flows), the grain-grain velocity would be lower than $U_w/10$, and then comparable to the velocity found previously[3,19].

In addition, some recent experimental works[63] showed velocity strengthening at high slip rates. This

strengthening of the friction coefficient is typically less than 0.1 while their weakening drop (from slow slip rate to high slip rate) is of 0.8 in the same experiments (note that our drop is similar: $\sim$0.7). This strengthening in the experiment at high velocity is therefore small. In addition, in our integrated approach, it will be difficult to observe such "high-rate" strengthening after the weakening phase. Finally, the number of landslides studied (and/or for which we can have access to the velocity) is limited compared to the numerous samples in the laboratory experiments. It is therefore difficult to distinguish between actual strengthening at high velocity and the scattering of the data set. Consequently these experimental observations are not in contradiction with our results presented here. These two last aspects have to be investigated more deeply in the future. They possibly lead to specific behaviours that could be identified in the field or in the generated seismic signal[17,64].

Supplementary References

[1] Cruden, D. M. & Varnes, D. J. Landslide types and processes. *Landslides Investigation and Mitigation Special Report 247. National Academy Press, pp 36–71*, (1996).

[2] Iverson, R. M., Logan, M., & Denlinger, R. Granular avalanches across irregular three-dimensional terrain: 2 experimental tests. *J. Geophys. Res.,* **109***, F01015*, (2004).

[3] Di Toro, G., Han, R., Hirose, T., De Paola, N., Nielsen, S., Mizoguchi, K., Ferri, F., Cocco, M., & Shimamoto, T. Fault lubrication during earthquakes. *Nature,* **471***, 494–498*, (2011).

[4] Hungr, O. Mobility of rock avalanches. *Report of the Nat. Research Inst. For Earth Science and Disaster Prevention, Tsukuba, Japan,* **46***, pp. 11–20*, (1981).

[5] Crosta, G. B., Frattini, P., & Fusi, N. Fragmentation in the Val Pola rock avalanche, Italian Alps. *J. Geophys. Res.,* **112***, F01006*, (2007).

[6] Kelfoun, K. & Druitt, T. H. Numerical modeling of the emplacement of Socompa rock avalanche, Chile. *J. Geophys. Res.,* **110***, B12202*, (2005).

[7] Singer, K., McKinnon, W., Schenk, P., & Moore, J. Massive ice avalanches on Iapetus caused by friction reduction during flash heating. *Nature Geoscience,* **5***(8), 574–578*, (2012).

[8] Schenk, P. & Bulmer, M. H. Thrust faulting, block rotation and large-scale mass movements at Euboea Montes, Io. *Science,* **279***(5356), 1514–1517*, (1998).

[9] Otto, A., Jaumann, R., Krohn, K., Matz, K.-D., Preusker, F., Roatsch, T., Schenk, P., Scholten, F., Stephan, K., Raymond, C., & Russell, C. Mass-wasting features and processes in Vesta's south polar basin Rheasilvia. *J. Geophys. Res. Planets,* **118***(11), 2279–2294*, (2013).

[10] King, J. P. Natural terrain landslide study - The natural terrain landslide inventory. *GEO Report No. 74. Hong Kong SAR: Geotechnical Engineering Office*, (1999).

[11] Sosio, R., Crosta, G. B., & Hungr, O. Complete dynamic modeling calibration for the Thurwieser rock avalanche (Italian Central Alps). *Engineering Geology,* **100***, 1-2, 11–26*, (2008).

[12] Lucas, A., Mangeney, A., Mège, D., & Bouchut, F. Influence of the scar geometry on landslide dynamics and deposits: Application to martian landslides. *J. Geophys. Res. - Planets,* **116***, E10001*, (2011).

[13] Shreve, R. L. Blackhawk landslide, southwestern San Bernardino County, California. *Geological Society of America Centennial Field Guide-Cordilleran Section, 109–114*, (1987).

[14] Voight, B., Janda, R., Glicken, H., & Douglass, P. Nature and mechanics of the mount St. Helens rockslide-avalanche of May 1980. *Geotechnique,* **33***, 243–273*, (1983).

[15] Young, S. R., Sparks, R. S. J., Aspinall, W. P., Lynch, L. L., Miller, A. D., Robertson, R. E. A., & Shepherd, J. B. Overview of the eruption of soufriere hills volcano, montserrat, 18 july 1995 to december 1997. *Geophys. Res. Lett.,* **25***(18), 3389–3392*, (1998).

[16] Mangeney, A., Roche, O., Hungr, O., Mangold, N., Faccanoni, G., & Lucas, A. Erosion and mobility in granular collapse over sloping beds. *J. Geophys. Res. - Earth Surface,* **115***, F03040*, (2010).

[17] Moretti, L., Mangeney, A., Capdeville, Y., Stutzmann, E., Huggel, C., Schneider, D., & Bouchut, F. Numerical modeling of the Mount Steller landslide flow history and of the generated long period seismic waves. *Geophys. Res. Lett.,* **39***, L16402*, (2012).

[18] Hibert, C., Mangeney, A., Grandjean, G., & Shapiro, N. Slopes instabilities in the Dolomieu crater, la Réunion island : from the seismic signal to the rockfalls characteristics. *J. Geophys. Res. - Earth Surface,* **116***, F04032*, (2011).

[19] Rice, R. J. Heating and weakening of faults during earthquake slip. *J. Geophys. Res.,* **111***, B05311.*, (2006).

[20] Legros, F. The mobility of long-runout landslides. *Eng. Geol.,* **63***, 301–331*, (2002).

[21] Heim, A. Bergsturz und Menschenleben. *Zurich: Fretz and Wasmuth*, (1932).

[22] Iverson, R. The physics of debris flows. *Reviews of Geophysics,* **35***, 245–296*, (1997).

[23] Lucas, A., Mangeney, A., Bouchut, F., Bristeau, M. O., & Mège, D. Benchmark excercices for granular flows. *In: Ho, K., Li, V. (Eds.) Proceedings of the 2007 International Forum on Landslide Disaster Management, Hong Kong*, (2007).

[24] Malin, C. M. Mass movements on Venus: Preliminary results from Magellan cycle 1 observations. *J. Geophys. Res.,* **97***(E10), 16337–16352*, (1992).

[25] Moore, M., Asphaug, E., Morrison, D., Spencer, J. R., Chapman, C. R., Bierhaus, B., Sullivan, R. J., Chuang, F. C., Klemaszewski, J. E., Greeley, R., Bender, K. C., Geissler, P. E., Helfenstein, P., & Pilcher, C. B. Mass movement and landform degradation on the icy Galilean satellites: Results of the Galileo nominal mission. *Icarus,* **140***(2), 294–312*, (1999).

[26] Quantin, C., Allemand, P., & Delacourt, C. Morphology and geometry of Valles Marineris landslides. *Planet. Space Sci.,* **52***, 1011–1022*, (2004).

[27] Kite, E. S., Lucas, A., & Fassett, C. I. Pacing early Mars river activity: Embedded craters in the aeolis dorsa region imply river activity spanned >(1-20) Myr. *Icarus,* **225***(1), 850–855*, (2013).

[28] Neukum, G. & Jaumann, J. HRSC: The High Resolution Stereo Camera of Mars Express, in Mars Express: The scientific payload. *The Scientific Payload, ESA, SP-1240, pp. 17–34*, (2004).

[29] Roche, O., Attali, M., Mangeney, A., & Lucas, A. On the run out distance of geophysical gravitational flows: insight from fluidized granular collapse experiments. *Earth Planet. Sci. Lett.,* **311***, 375–385*, (2011).

[30] Lucas, A. & Mangeney, A. Mobility and topographic effects for large valles marineris landslides on Mars. *Geophys. Res. Lett.,* **34***, L10201*, (2007).

[31] Mangeney, A., Heinrich, P., & Roche, R. Analytical solution for testing debris avalanche numerical models. *Pure Appl. Geophys.,* **157***, 1081–1096*, (2000).

[32] Kerswell, R. R. Dam break with coulomb friction: A model of granular slumping? *Phys. Fluids,* **17***, 057101*, (2005).

[33] Faccanoni, G. & Mangeney, A. Exact solution for granular flows. *Int. J. Num. Analy. Meth. Goemech.,* **37***(10), 1408–1433*, (2013).

[34] Pouliquen, O. & Forterre, Y. Friction law for dense granular flows: Application to the motion of a mass down a rough inclined plane. *J. Fluid Mech.,* **453***, 133–151*, (2002).

[35] Mangeney-Castelnau, A., Bouchut, F., Vilotte, J. P., Lajeunesse, E., Aubertin, A., & Pirulli, M. On the use of Saint-Venant equations to simulate the spreading of a granular mass. *J. Geophys. Res.,* **110***, B09103*, (2005).

[36] Staron, L. & Lajeunesse, E. Understanding how volume affects the mobility of dry debris flows. *Geophys. Res. Lett.,* **36***, L12402*, (2009).

[37] Crosta, G. B., Imposimato, S., & Roddeman, D. Numerical modeling of 2-D granular step collapse on erodible and nonerodible surface. *J. Geophys. Res.,* **114***, F03020*, (2009).

[38] Davies, T. R. Spreading of rock avalanche debris by mechanical fluidization. *Rock mechanics, June 1982,* **15***(1), 9–24*, (1982).

[39] Lube, G., Huppert, H., Sparks, R., & Hallworth, M. A. Axisymmetric collapses of granular columns. *J. Fluid Mech.,* **508***, 175*, (2004).

[40] Lajeunesse, E., Mangeney-Castelnau, A., & Vilotte, J. Spreading of a granular mass on an horizontal plane. *Phys. Fluids,* **16***(7), 2371–2381*, (2004).

[41] Erismann, T. Mechanisms of large landslides. *Rock Mechanics,* **12***, 15–46*, (1979).

[42] Melosh, H. J. Acoustic fluidization: A new geologic process? *J. Geophys. Res.,* **84***, 7513–7520*, (1979).

[43] Davies, T. R., McSaveney, M. J., & Hodgson, K. A. A fragmentation spreading model for long-runout rock avalanches. *Can. Geotech. J.,* **36***(6), 1096–1110*, (1999).

[44] Davies, T. R., McSaveney, M. J., & Beetham, R. D. Rapid block glides: Slide-surface fragmentation in New Zealand's Waikaremoana landslide. *Q. J. Eng. Geol. Hydrogeol.,* **39***, 115–129*, (2006).

[45] Hungr, O. & Evans, S. G. Entrainment of debris in rock avalanches: An analysis of a long runout mechanism. *Bull. Geol. Soc. Am.,* **116***, 1240–1252*, (2004).

[46] Goren, L. & Aharonov, E. Long runout landslides: The role of frictional heating and hydraulic diffusivity. *Geophys. Res. Lett.,* **34***, L07301*, (2007).

[47] Mangeney, A., Tsimring, L. S., Volfson, D., Aranson, I. S., & Bouchut, F. Avalanche mobility induced by the presence of an erodible bed and associated entrainment. *Geophys. Res. Lett.,* **34***, L22401*, (2007).

[48] De Blasio, F. V. Landslides in Valles Marineris (Mars): A possible role of basal lubrication by subsurface ice. *Planet. Space Sci.,* **59***, 1384–1392*, (2011).

[49] Viesca, R. & Rice, J. R. Nucleation of slip-weakening rupture instability in landslides by localized increase of pore pressure. *J. Geophys. Res.,* **B3***(117), 2156–2202*, (2012).

[50] Lucas, A. Slippery sliding on icy Iapetus. *Nature Geosci.,* **5***(8), 524–525*, (2012).

[51] Pudasaini, S. P. & Miller, S. A. The hypermobility of huge landslides and avalanches. *Engineering Geology,* **157***, 124–132*, (2013).

[52] Campbell, C., Clearly, P. W., & Hopkins, M. Large-scale landslide simulations: Global deformation, velocities and basal friction. *J. Geophys. Res.,* **100***(B5), 8267–8283*, (1995).

[53] Farin, M., Mangeney, A., & Roche, O. Fundamental changes of granular flow dynamics, deposition and erosion processes at high slope angles: insights from laboratory experiments. *J. Geophys. Res., Accepted Paper, doi:10.1002/2013JF002750*, (2013).

[54] Roche, O. e. a. Dynamic pore pressure variations induce substrate erosion by pyroclastic flows. *Geology,* **41***(10), 1107–1110*, (2013).

[55] Hirono, T. e. a. Clay mineral reactions caused by frictional heating during an earthquake: An example from the Taiwan Chelungpu fault. *Geophys. Res. Lett.,* **35***, L16303*, (2008).

[56] Brantut, N., Schubnel, A., Rouzaud, J.-N., Brunet, F., & Shimamoto, T. High-velocity frictional properties of a clay-bearing fault gouge and implications for earthquake mechanics. *J. Geophys. Res.,* **113***, B10401*, (2008).

[57] Brantut, N., Han, R., Shimamoto, T., Findling, N., & Schubnel, A. Fast slip with inhibited temperature rise due to mineral dehydration: evidence from experiments on gypsum. *Geology,* **39***(1), 59–62*, (2011).

[58] Brantut, N., Schubnel, A., Corvisier, J., & Sarout, J. Thermo-chemical pressurization of faults during coseismic slip. *J. Geophys. Res.,* **115***, B05314*, (2010).

[59] Beeler, N. M., Tullis, T. E., & Goldsby, D. L. Constitutive relationships and physical basis of fault strength due to flash heating. *J. Geophys. Res.,* **113***, B01401*, (2008).

[60] Goldsby, D. L. & Tullis, T. E. Flash heating leads to low frictional strength of crustal rocks at earthquake slip rates. *Science,* **334***, 216–218*, (2011).

[61] Kuwano, O. & Hatano, T. Flash weakening is limited by granular dynamics. *Geophys. Res. Lett.,* **38***, L17305*, (2011).

[62] Kennedy, F. E., Schulson, E. M., & Jones, D. E. The friction of ice on ice at low sliding velocities. *Philosophical Magazine A,* **80***:5, 1093–1110*, (2000).

[63] Chen, J. & Rempel, A. W. Flash heating and fault zone evolution. *AGU Fall Meeting, S21B-2453*, (2012).

[64] Favreau, P., Mangeney, A., Lucas, A., Crosta, G., & Bouchut, F. Numerical modeling of landquakes. *Geophys. Res. Lett.,* **37***, L15305*, (2010).